

# Label-Free Cellular Imaging by Broadband Coherent Anti-Stokes Raman Scattering Microscopy

Sapun H. Parekh, Young Jong Lee, Khaled A. Aamer, and Marcus T. Cicerone\*

Polymers Division, National Institute of Standards and Technology, Gaithersburg, Maryland

**ABSTRACT** Raman microspectroscopy can provide the chemical contrast needed to characterize the complex intracellular environment and macromolecular organization in cells without exogenous labels. It has shown a remarkable ability to detect chemical changes underlying cell differentiation and pathology-related chemical changes in tissues but has not been widely adopted for imaging, largely due to low signal levels. Broadband coherent anti-Stokes Raman scattering (B-CARS) offers the same inherent chemical contrast as spontaneous Raman but with increased acquisition rates. To date, however, only spectrally resolved signals from the strong CH-related vibrations have been used for CARS imaging. Here, we obtain Raman spectral images of single cells with a spectral range of 600–3200  $\text{cm}^{-1}$ , including signatures from weakly scattering modes as well as CH vibrations. We also show that B-CARS imaging can be used to measure spectral signatures of individual cells at least fivefold faster than spontaneous Raman microspectroscopy and can be used to generate maps of biochemical species in cells. This improved spectral range and signal intensity opens the door for more widespread use of vibrational spectroscopic imaging in biology and clinical diagnostics.

## INTRODUCTION

Imaging and image-based analysis have long been a workhorse of biological and clinical investigation. Methods such as bright field and phase contrast are completely noninvasive, but provide minimal biochemical information. Fluorescence microscopy can provide real-time, spatially resolved information about biological structures and chemical species, making it an indispensable tool for cell biology and physiology studies. However, fluorescence imaging presents potential complications from nonnative fluorescent probes and fusion protein tags, affecting molecular function and cytotoxic free-radical generation. In addition, the useful lifetime of a fluorescence experiment is always limited by photobleaching of the probe.

Spontaneous Raman scattering microscopy derives contrast from the inherent molecular composition of the sample, and offers a label-free, high-resolution imaging that can provide tremendously rich chemical and spatial information. Together, the chemical information in the fingerprint (500–1600  $\text{cm}^{-1}$ ) and CH-stretch (2840–3000  $\text{cm}^{-1}$ ) regions of Raman spectrum has been used to localize cellular organelles such as mitochondria, nuclei, and chromatin (1–3), detect differentiation of stem cells (4,5), discriminate among subtly different cell (6,7) and tissue types (8), and characterize and stratify cancerous tissues with high sensitivity and selectivity (9,10).

Given its apparent advantages and high information content, it is remarkable that Raman microspectroscopy is not used more widely as a tool for characterization of cells and tissues. While advantageous in terms of label-free

imaging and characterization, spontaneous Raman microspectroscopy has significant limitations due to intrinsically weak Raman scattering. Even when the laser power is applied near the physical damage threshold, spectral acquisition requires times ranging from 250 ms to minutes per spatial pixel (2,3,5,11–13). The long acquisition time makes routine imaging applications impractical, and the high laser powers make truly noninvasive cellular imaging nearly impossible (14). A further complication of spontaneous Raman spectroscopy is the presence of a spectrally overlapping autofluorescence from the sample and substrate, the shot noise of which can dominate the weaker Raman scattering. In this article, we present a coherent Raman imaging technique that overcomes many limitations of spontaneous Raman scattering described above and provides broad spectral bandwidth to sample an equivalent spectral window.

Coherent anti-Stokes Raman scattering (CARS) is a nonlinear multiphoton phenomenon in which the signal is enhanced by vibrational resonance. CARS signals contain the same inherent vibrational information as spontaneous Raman spectroscopy. It offers potential advantages of reducing acquisition time and minimal interference with fluorescence light. CARS uses a two-photon excitation scheme with a pump photon ( $\omega_{\text{pump}}$ ) and Stokes photon ( $\omega_{\text{Stokes}}$ ) coherently interacting to excite a vibrationally resonant mode ( $\Delta\nu_{\text{vib}} = \omega_{\text{pump}} - \omega_{\text{Stokes}}$ ) in a sample. A third (probe) photon ( $\omega_{\text{probe}}$ ) is inelastically scattered off this coherent excitation, and anti-Stokes light ( $\omega_{\text{as}} = \omega_{\text{pump}} - \omega_{\text{Stokes}} + \omega_{\text{probe}}$ ) is emitted from the sample. CARS emission is blue-shifted relative to all excitation beams and thus spectrally removed from any linear fluorescence emission. Furthermore, because CARS is a multiphoton process, it offers optical sectioning similar to two-photon fluorescence microscopy (15,16). Perhaps most importantly,

Submitted June 14, 2010, and accepted for publication August 10, 2010.

\*Correspondence: cicerone@nist.gov

Editor: Alberto Diaspro.

© 2010 by the Biophysical Society  
0006-3495/10/10/2695/10 \$2.00

doi: 10.1016/j.bpj.2010.08.009

because CARS is a coherent excitation process, the signal can be up to  $10^6$ -fold larger than spontaneous Raman scattering, resulting in significant speed improvements (17).

By far the most popular CARS technique in bioimaging is single frequency CARS microscopy, originally pioneered by Duncan et al. (18) and later revived by Zumbusch et al. (19). The single frequency approach is capable of acquiring label-free images at video rates, and its clinical adaption is underway (15,20). In this configuration, the pump and Stokes wavelengths are tuned to excite a single vibrational resonance, usually in the CH-stretch region of the spectrum ( $2840\text{--}3000\text{ cm}^{-1}$ ), which is extremely useful for tissue and cellular samples due to abundance of lipids and membranes. However, single-frequency CARS microscopy is not useful for distinguishing components with subtle differences in chemical composition that, for example, may be apparent only through a ratio of multiple peak intensities.

Another approach is multiplex CARS (M-CARS) microscopy, where a spectrally broad femtosecond pulse is used for the Stokes transition, providing sensitivity over  $300\text{--}1500\text{ cm}^{-1}$  of spectral bandwidth at each spatial pixel (21–26). M-CARS has been used to characterize neat liquids, polymer blends, domains in lipid droplets, and bacterial spores (26–28). Rinia et al. (26) and Bonn et al. (27) used M-CARS microscopy ( $300\text{ cm}^{-1}$  bandwidth) to investigate the domain variability and extent of saturated fatty acid content in cellular lipid droplets. Petrov et al. (28) and Pestov et al. (29) have used a similar laser system to the one described here to produce high quality M-CARS spectra ( $1500\text{ cm}^{-1}$  bandwidth) of bacterial spores with significantly shorter acquisition times than with confocal Raman spectroscopy. However, the bandwidth of M-CARS microscopy is insufficient to simultaneously acquire fingerprint and CH-stretch signals. Acquiring both signals would provide chemical information that can be used for discriminating normal from pathological tissue and differentiating between cell types, but has not been demonstrated. Broadband CARS (B-CARS) microscopy has sufficient bandwidth ( $500\text{--}3200\text{ cm}^{-1}$ ) for these purposes. Until recently, the primary roadblock preventing full-spectral B-CARS microscopy in biological samples has been a lack of appropriate laser sources that provide sufficient power and spectral breadth. We recently demonstrated an appropriate supercontinuum source that has overcome this limitation (30).

While the CARS signal intensity is dramatically enhanced compared to spontaneous Raman scattering, resonant Raman peaks in a CARS spectrum are accompanied by nonresonant background (NRB) that very often dominates the weaker resonant signals of interest. Unlike spontaneous Raman spectroscopy where the fluorescence background that spectrally overlaps with Raman signals can be subtracted from the detected signal, the NRB in CARS interferes coherently with the resonant signal, resulting in a dispersive line shape and amplitude that is not related in a simple way to analyte concentration. Many sophisticated

optical schemes have been devised to minimize the NRB contribution to the measured CARS spectrum (30,31,32). However, in each case overall CARS signal strength is sacrificed, which can adversely affect the signal-to-noise (S/N) ratio of the detected CARS spectrum. Furthermore, it is unclear whether these arrangements will function appropriately in complex biological samples.

Though the NRB does distort the spectral shape, it also serves to amplify the resonant signal component through a heterodyne interaction (see Eq. 1 below). This amplification factor can be exploited by using the NRB for signal generation, then separating the resonant and nonresonant components after the signal is detected. Two computational methods, a modified Kramers-Kronig (KK) transform, and a maximum entropy approach, have been used to retrieve the resonant signal of interest from the NRB in M-CARS and B-CARS spectra (33,34). These computational methods have been demonstrated in M-CARS biological applications (described above) and B-CARS spectroscopy of neat liquids (34). The rapid, high-fidelity extraction of the resonant component from the raw CARS signal afforded by the KK transform was crucial for obtaining the spectral images shown here.

In this article, we demonstrate a B-CARS imaging technique that produces complete resonant vibrational spectra of single cells with 50-ms individual pixel dwell times. This acquisition time is at least fivefold faster than spontaneous confocal Raman microspectroscopy of cells at similar spatial resolution based on acquisition speeds reported in the literature (2,3,5,11–13). The B-CARS vibrational spectra covers the range  $600\text{--}3200\text{ cm}^{-1}$ , encompassing both the fingerprint and CH-stretch regions in a single measurement without spectral scanning and providing both morphological and rich biochemical information simultaneously. This technique is capable of providing spatiochemical maps of single cells with increased speed and spectral breadth compared to existing vibrational imaging modes. In this first demonstration of B-CARS microscopy on cells, we demonstrate that we can chemically localize nuclei in the heterogeneous intracellular environment by showing that the nuclear regions of cells identified by B-CARS imaging colocalize well with fluorescence images.

## MATERIALS AND METHODS

### Cell culture

L929 mouse fibroblasts were obtained from the American Type Cell Culture facility (cat. No. CCL-1; ATCC, Manassas, VA) and grown in Minimum Essential Media (cat. No. 10370-021; Invitrogen, Carlsbad, CA) supplemented with 10 % fetal bovine serum (cat. No. 26140; Gibco, Billings, MT), 2 mmol/L L-glutamine (cat. No. 25030; Invitrogen), and 1 mmol/L sodium pyruvate (cat. No. 11360-070; Invitrogen). Passage-2 cells were thawed from a liquid nitrogen dewar and grown to confluency on tissue culture-treated polystyrene before replating onto ethanol and flame-sterilized glass No. 1 coverslips (ThermoFisher, Waltham, MA) for B-CARS imaging. All cells used for this study were passage 3–6.

## Cellular fixation, staining, and mounting

For B-CARS imaging without fluorescence, cells were initially fixed in 3.7 % formaldehyde (% by volume) in nonsterile Dulbecco's phosphobuffered saline (DPBS, cat. No. 14040; Gibco) without  $\text{CaCl}_2$  or  $\text{MgCl}_2$ . Cells were lightly fixed by adding the formaldehyde solution in equal volume (as the media) to the cells and incubating for 10 min at room temperature. After aspiration of this solution, cells were incubated in formaldehyde solution alone for another 10 min at room temperature, rinsed three times with DPBS and stored in DPBS for up to two days at room temperature. All cells were imaged within two days of fixing to avoid any degradation or contamination over time.

For nuclear staining, fixed cells on coverslips were incubated with a 1  $\mu\text{g}/\text{mL}$  solution of Hoechst 33342 (cat. No. H21492; Invitrogen) for 5 min at room temperature under light agitation. The dye solution was then washed out three times with DPBS. Coverslips were mounted to glass slides for imaging by using two pieces of double-sided tape to form a  $\approx 65\text{-}\mu\text{m}$ -thick channel so as to not squash the cells against the two glass surfaces. The channel was filled with DPBS and sealed with vaseline-alanin-paraffin wax before imaging.

## B-CARS imaging system

The essential elements of our B-CARS imaging system are shown in Fig. 1, and the current system has been described in detail previously (30). Our B-CARS imaging system is built around a Mai Tai laser (Spectra-Physics, Mountain View, CA) operating at  $\lambda_c = 830\text{ nm}$  (37.5 nJ/pulse, 80 MHz) with the DeepSee pulse compression unit (MaiTai, Spectra-Physics). This oscillator pulse was split into two parts: one used for supercontinuum generation in a photonic crystal fiber (FemtoWHITE, NKT Photonics, Morganville, NJ) for the Stokes pulse (850–1200 nm), and the other used to prepare a narrowband probe pulse centered at 830 nm (21,30). The supercontinuum output was stabilized by a feedback-controlled three-axis stage (model No. MAX301; Thorlabs, Newton, NJ) and was collimated by a parabolic mirror (model No. 50328AL; Newport Corporation, Irvine, CA). The probe beam was spectrally narrowed using a reflective-type 4- $f$  dispersion-less filter consisting of a grating (cat. No. 10RG1200-1000-2; Newport), achromatic lens (model No. AC254-200-B; Thorlabs), and a slit (model No. SV-0.5; Newport) to select 830 nm light with a  $10\text{ cm}^{-1}$  bandwidth. The probe and Stokes beams were combined and fed into the laser port of a model No. IX-71 microscope (Olympus, Melville, NY) where they were focused into the sample plane using either a 60 $\times$ , 1.35 NA UPlanApo oil immersion or 60 $\times$ , 1.2 NA water immersion objective (Olympus). The B-CARS signal was detected and collimated in the forward direction with a 60 $\times$ , 0.7 NA PlanApo objective (Olympus) and directed into a monochromator (Acton 2300; Princeton Instruments, Trenton, NJ) that dispersed the light onto a cooled ( $-70^\circ\text{C}$ ) deep depletion charge-coupled device (CCD model No. BRDD-920; Andor Technology, Belfast, Northern Ireland). The uncertainty in our monochromator calibration is  $5.7\text{ cm}^{-1} \pm 2.1\text{ cm}^{-1}$  (mean  $\pm$  SD), and the spectral resolution of our CARS instrument is  $9.5\text{ cm}^{-1} \pm 1\text{ cm}^{-1}$  (mean  $\pm$  SD). The timing between the Stokes and probe pulses was optimized for maximal B-CARS signal generation from the buffer surrounding the cells in the sample (Fig. 2 A, blue trace).

B-CARS images were collected by scanning the sample with a computer-controlled stage (model No. MS 2000; Applied Scientific Instrumentation, Eugene, OR) and acquiring full resolution spectra at each pixel in the scan. The synchronization and acquisition are controlled by custom software written in LabView 7.1 (National Instruments, Austin, TX).

## B-CARS data analysis

B-CARS data is saved by the acquisition software for offline processing with Igor Pro 5.05A (WaveMetrics, Lake Oswego, OR). The resonant signal extraction, based on a modified Kramer-Kronig transform, is described in detail elsewhere (34) and has been integrated into a larger analysis suite

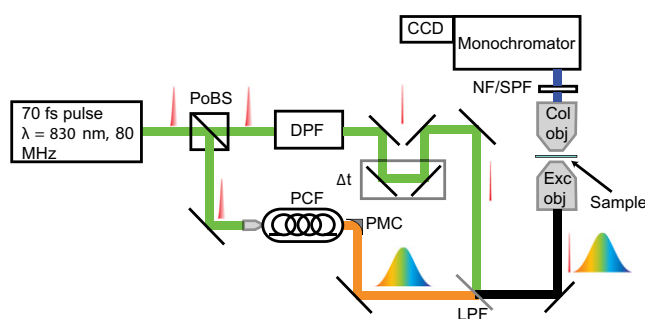


FIGURE 1 Schematic of B-CARS microspectroscopy setup. Light from a Spectra Physics MaiTai laser ( $\lambda = 830\text{ nm}$ ) is split into two paths by a polarization beam splitter (PoBS): one for generating a broadband continuum in a photonic crystal fiber (PCF) and the other to pass through a dispersion-less filter (DPF) to prepare a narrowband ( $10\text{ cm}^{-1}$ ) probe pulse (Gaussian shapes illustrate spectral widths). The continuum pulse is collimated with a parabolic mirror (PMC) and the two beams are combined by a long-pass filter (LPF) before injection into the microscope. The excitation and collection objectives are arranged with a coincident focus, and the B-CARS signal is separated from the excitation light beams by a notch (NF) and short-pass filter (SPF). B-CARS light is dispersed by a monochromator onto a cooled charge-coupled device (CCD) for spectral acquisition. Timing between the two pulses is controlled by a delay stage in the probe beam path such that B-CARS intensity is maximized. An automated, computer-controlled stage moves the sample relative to the excitation beams to obtain B-CARS spectra from different spatial pixels in the sample to facilitate subsequent vibrational image construction.

for data processing. Obtaining an accurate representation of the NRB at each spatial pixel is crucial to reliable resonant extraction. To accomplish this, spatial regions of the B-CARS image-containing cells are masked based on physical contrast (changes in the NRB level), and the mask is used to select the cell-free areas of the image to calculate an averaged NRB. Spectra from pixels outside the mask are averaged line-by-line to obtain a line-averaged NRB signal. The resonant signal from each pixel is then extracted using the line-averaged NRB from same line.

After resonant extraction, any residual, slowly varying spectral baseline due to variance of the line-averaged NRB signal from the actual NRB at a given pixel is removed by fitting the overall baseline shape to two disparate regions of the extracted spectrum ( $\approx 500\text{--}800\text{ cm}^{-1}$  and  $1700\text{--}2700\text{ cm}^{-1}$ ) with a third-order polynomial. The fitted curve is subtracted from the extracted resonant spectrum on a pixel-by-pixel basis to detrend the data. This detrending is necessary for reliable qualitative or quantitative analysis of the spectral images, and is similar to processes commonly used in spontaneous Raman and M-CARS spectral analyses (26,35). The extracted and detrended data is used for all subsequent spectral analysis.

Multivariate analysis was done with Solo+MIA software (Eigenvector Research, Wenatchee, WA). Extracted and detrended data was loaded in the multivariate analysis software. Spectra were differentiated using a 15-point, fourth-order Savitzky-Golay filter before performing a principal component analysis. The loadings on the first and second principal components were plotted as seen later in Fig. 4 D.

## RESULTS

In our system, we use a narrowband pump (and probe) and broadband Stokes pulse in the two-color configuration to obtain B-CARS spectra at each spatial pixel with a spectral range of  $600\text{--}3200\text{ cm}^{-1}$ . Fig. 2 A shows raw B-CARS spectra from a single location in a cell and in the surrounding buffer solution. As mentioned in the Introduction,

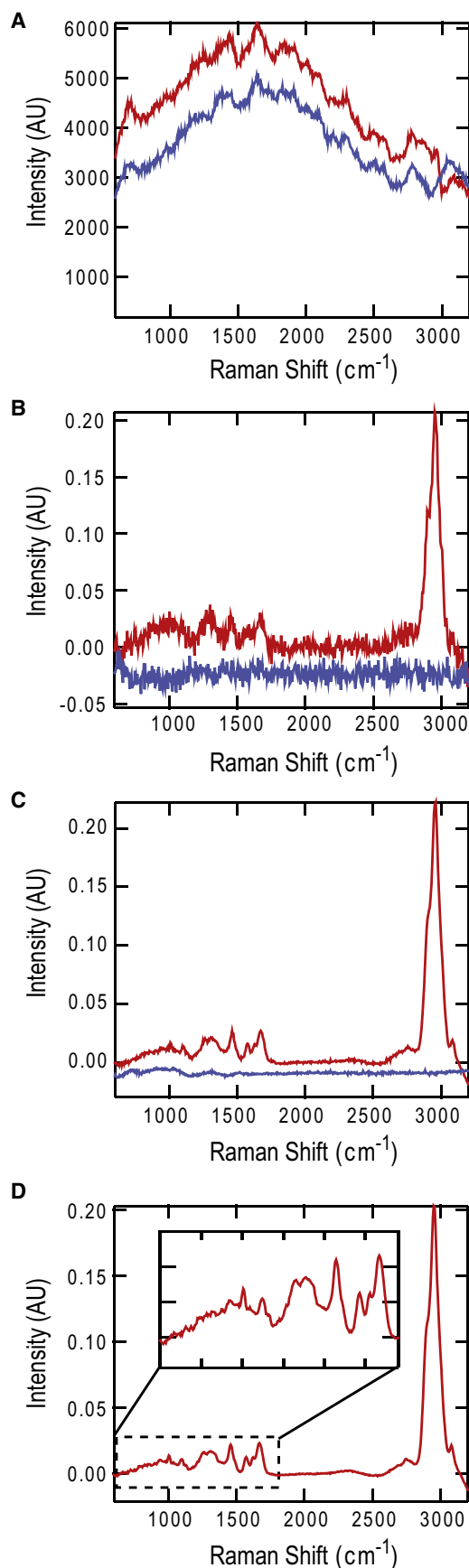


FIGURE 2 B-CARS spectroscopy of a single L929 mouse fibroblast cell. (A) Raw CARS spectrum from a single pixel inside the cell (*red*) and outside the cell (*blue*). (B) After resonant signal extraction, the spectrum from inside the cell (*red*) shows the commonly seen CH-stretch peak ( $\approx 2900\text{ cm}^{-1}$ ) as well as information in the fingerprint region of the spectrum. The PBS area outside the cell (*blue*) shows no resonant peaks, demonstrating that our signal extraction can effectively remove the nonresonant background from raw CARS spectra while preserving the vibrationally resonant signal. (C) Average of resonant-extracted spectra over a  $9 \times 9$  pixels ( $5.06\text{ }\mu\text{m}^2$ ) in the cell (*red*) and in PBS (*blue*). (D) Average of resonant-extracted spectra over the entire cell. (*Inset*) The fingerprint region of the spectrum shows numerous peaks that have been identified by spontaneous Raman spectroscopy ( $1003, 1095, 1445, 1487, 1578, 1602,$  and  $1660\text{ cm}^{-1}$  among others). The laser powers were set to 22 mW (Stokes) and 20 mW (Probe) at the sample plane, and the exposure time for each pixel ( $250\text{ nm} \times 250\text{ nm}$ ) was 50 ms.

resonant Raman modes have a dispersive line shape in CARS spectra and the sharp resonant Raman features of the sample ride on top of a coherent NRB signal (28,36,37). The NRB field adds to the resonant CARS field such that the detected intensity contains both components in addition to a cross term

$$I_{\text{CARS}}(\omega) \propto |E_{\text{NRB}}(\omega)|^2 + 2^*E_{\text{NRB}}(\omega) * \text{Re}\{E_{\text{Res}}(\omega)\} + |E_{\text{Res}}(\omega)|^2, \quad (1)$$

where  $E_{\text{NRB}}$  and  $E_{\text{Res}}$  are the NRB and resonant fields, respectively. Typically, the first term on the right side of Eq. 1 dominates the CARS signal, making it difficult to directly observe the resonant features of the sample. This is shown by the raw B-CARS data in Fig. 2 A, where only subtle differences can be seen between the raw B-CARS data from pixels in the cell (Fig. 2 A, *red trace*) and buffer (Fig. 2 A, *blue trace*).

Experimental approaches to suppress the NRB have been successful for high concentration analytes in solution where the resonant field (third term in Eq. 1) is relatively strong, so the detected intensity is still quite large. However, in cellular samples, signals not associated with CH vibrations are very weak, and the cross-term in Eq. 1 serves to boost the resonant CARS signal intensity sufficiently that it can be extracted computationally. Computational methods from our group (34,38) as well as others (24,33,39) have been demonstrated to extract the resonant signal from raw CARS spectra. The method employed here, described in detail by Liu et al. (34), uses the principle of causality, embodied in a KK transform, and makes accommodation for a temporally finite excitation pulse. Practically, by comparing the raw CARS signal and an NRB from the same location (both Fourier-transformed into the time domain), we can calculate the imaginary part of the resonant signal, which is the same quantity as measured with spontaneous Raman spectroscopy (40). A typical extraction takes  $<3$  ms for each spatial pixel in the image, and resonant B-CARS hyperspectral data are obtained in  $<1.2$  min for  $151 \times 151$  spatial pixels with  $\approx 600$  spectral points at each spatial location.

Once processed for resonant signal extraction, the spectrum from each individual pixel no longer has the dominant NRB envelope that masks the sharp vibrationally resonant features. Instead, the spectra resemble data that are obtained from spontaneous Raman spectroscopy (Fig. 2 B) (3). The data from a single pixel in the cell (Fig. 2 B, red trace) shows characteristic resonances at  $1440\text{ cm}^{-1}$ ,  $1660\text{ cm}^{-1}$ , and at  $2900\text{ cm}^{-1}$ , which correspond to the  $\text{CH}_2$ -def, amide I ( $\text{C}=\text{C}$ ), and CH-stretch regions of the spectrum, respectively, with virtually no baseline. Fig. 2 B also shows the spectrum from a pixel in the surrounding PBS (blue trace) after resonant signal extraction. This trace shows no characteristic sharp features, which is consistent with the spontaneous Raman spectrum from PBS (41). This demonstrates that our linewise NRB averaging and signal extraction method accurately removes the spectrally broad and dominating NRB signal while preserving the vibrationally resonant Raman features.

The traces in Fig. 2 B are from single pixels. These traces, although noisy, are identifiable as Raman spectra. By averaging neighboring spatial locations in the cell, we can obtain higher S/N spectra. Fig. 2 C shows a spectrum produced by averaging 81 spatial pixels, which is similar to spontaneous Raman spectra of individual cells (Fig. 2 C) (1,3,12,42). Compared to the 81 pixel-averaged spectrum, no significant increase in S/N is seen upon further averaging over the entire cell body ( $n = 1700$  pixels, Fig. 2 D). A detailed discussion of the amount of averaging required to obtain a desired S/N for a specific vibrational resonance is presented later (see Discussion). Even for relatively weak modes such as the  $785\text{ cm}^{-1}$ , a measurement of  $S/N \approx 1$  can be obtained from averaging as few as four neighboring pixels (see later in Fig. 5 D). The fingerprint features shown in Fig. 2, C and D, can be assigned to specific vibrational modes based on their common appearance in spontaneous Raman spectra of cells. Resonances from the phosphate in the DNA backbone ( $1095\text{ cm}^{-1}$ ), nucleotide bases ( $1487\text{ cm}^{-1}$  and  $1578\text{ cm}^{-1}$ ), phenylalanine in proteins ( $1003\text{ cm}^{-1}$ ), and the amide I in peptide bonds ( $1660\text{ cm}^{-1}$ ) are clearly visible in addition to many other fingerprint peaks (Fig. 2 D, inset) (6,12). This is, to our knowledge, the first demonstration of full bandwidth ( $600\text{--}3200\text{ cm}^{-1}$ ) vibrational spectra acquired with B-CARS microscopy from a single cell.

In addition to obtaining resonant broadband vibrational spectra from entire cells, our B-CARS technique allows spatial mapping of specific chemical species within a cell faster than by using spontaneous confocal Raman microscopy with similar spatial resolution (1,2,13). In Fig. 3, we show a bright-field image of a cell (Fig. 3 A) along with an image created from the CH-stretch region of the spectrum, specifically  $2900\text{ cm}^{-1}$  (Fig. 3 B). From Fig. 3 A, we see vacuoles or fat droplets that have been seen previously on L929 cells cultured on glass coverslips (43) and in National Institutes of Health (NIH) 3T3 cells (44) with

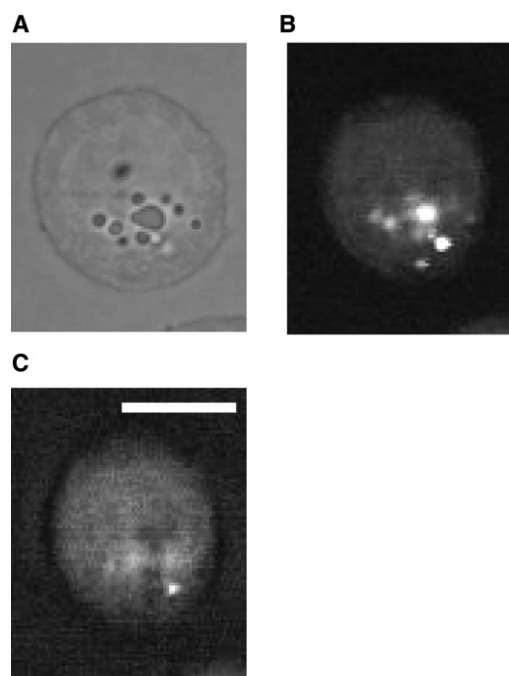
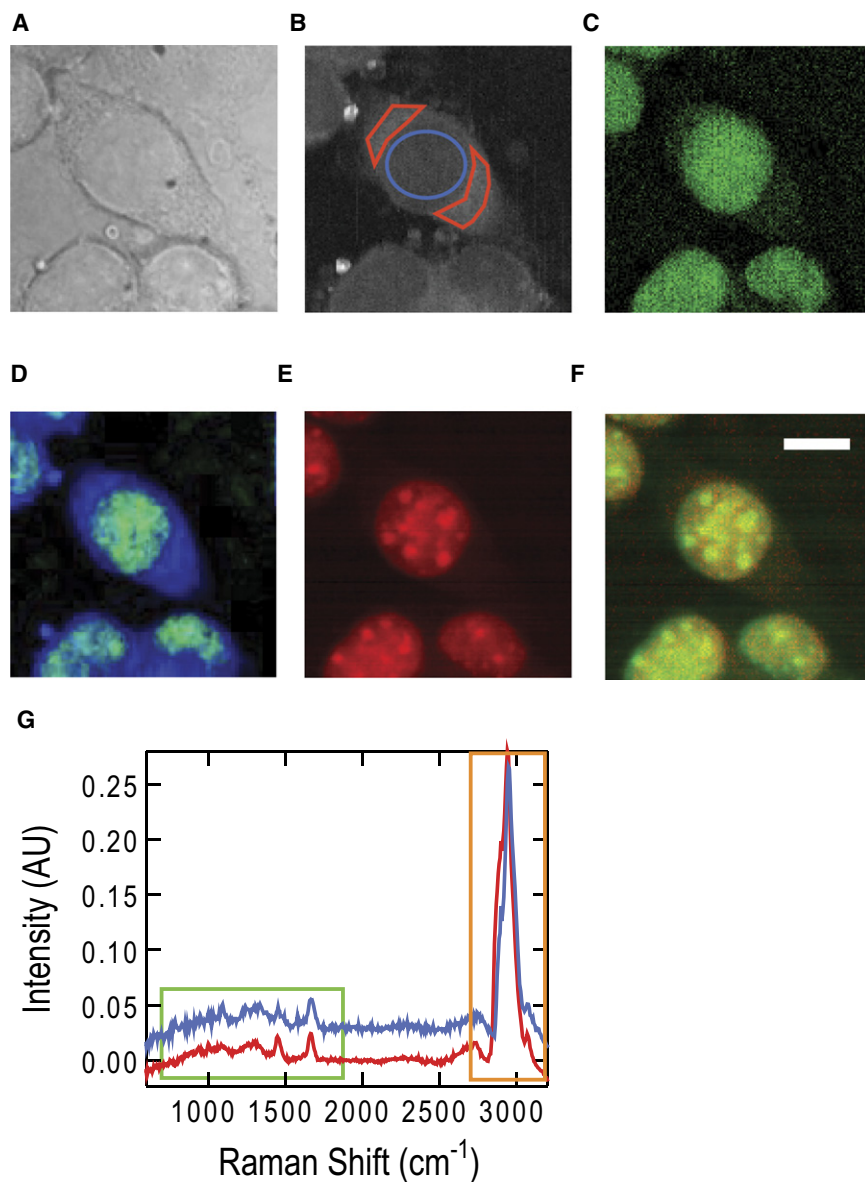


FIGURE 3 Raman imaging of L929 cells obtained with B-CARS microscopy. (A) Bright-field image of the L929 cell. (B) Raman image of the cell created from the resonant-extracted signal intensity at  $2900\text{ cm}^{-1}$ . (C) Raman image created from resonant-extracted signal intensity at  $1660\text{ cm}^{-1}$ . Experimental conditions were the same as Fig. 2. Scale bar =  $10\text{ }\mu\text{m}$ .

single frequency CARS microscopy. The CH-stretch image from Fig. 3 B shows very bright intensities colocalizing with droplets in the bright-field image, verifying the appearance of lipid droplets in the fibroblast cell. An image constructed from the amide I ( $\text{C}=\text{C}$ ) band,  $1660\text{ cm}^{-1}$  (Fig. 3 C), shows that the lipid droplets do not contain a high degree of unsaturation relative to the surrounding cytoplasm.

While B-CARS microscopy allows image construction from single frequency intensities as shown in Fig. 3, we can also use the hyperspectral vibrational dataset to construct chemical images based on multiple spectral components to highlight cellular organelles. Fig. 4 A is a bright-field image showing a group of fibroblasts, which is essentially reproduced by the resonant B-CARS image from intensities at  $2900\text{ cm}^{-1}$  (Fig. 4 B). Upon inspecting spectra from regions of the cell that morphologically appear to be nuclei, we notice both fingerprint and CH-stretch differences between nuclear and cytoplasmic regions (Fig. 4 G). By subtracting the resonant-extracted signal intensity of  $2853\text{ cm}^{-1}$  from the intensity at  $3003\text{ cm}^{-1}$ , we generate contrast to exclusively highlight the nuclei of these cells (Fig. 4 C). In addition, using a principal component analysis of first derivative spectra, a similar nuclear image can be generated (Fig. 4 D). Comparing the image generated in Fig. 4 C with an image of the Hoechst-stained fluorescent of DNA (Fig. 4 E), we validate the nuclear specificity of the chemical image generated in Fig. 4 C. An overlay of the fluorescent and B-CARS nuclear images



**FIGURE 4** B-CARS chemical imaging of cell nuclei. (A) Bright-field image of L929 cells. (B) Raman image constructed from resonant-extracted B-CARS signal at  $2900\text{ cm}^{-1}$ . (C) Image constructed from difference in B-CARS resonant-extracted signal intensity between  $3003\text{ cm}^{-1}$  and  $2853\text{ cm}^{-1}$  generates chemical contrast highlighting the nuclear regions of the cell. (D) Image of cell nuclei (*green*) and cytosol (*blue*) generated by principal component analysis of resonant-extracted B-CARS data (see Materials and Methods). (E) Fluorescent image of Hoechst-stained DNA in the same cells. (F) Overlay of images from panels C and E demonstrates accurate nuclear identification using B-CARS microscopy. (G) Spectra generated by averaging extracted spectra from  $n = 751$  and  $731$  pixels in nuclear and cytoplasmic regions of the cell, respectively. Regions of interest in panel B are color-coded traces and traces are vertically offset for clarity. The laser powers were set to  $20\text{ mW}$  (Stokes) and  $20\text{ mW}$  (Probe) at the sample plane, and the exposure time for each pixel ( $300\text{ nm} \times 300\text{ nm}$ ) was  $50\text{ ms}$ . Scale bar =  $10\text{ }\mu\text{m}$ .

(Fig. 4 F) demonstrates that B-CARS imaging can be used to noninvasively identify cellular nuclei with high specificity.

Averaging retrieved spectra over nuclear and cytoplasmic regions of the center cell in Fig. 4 A shows clear differences in the spectra (Fig. 4 G). In the nuclear region of the cell, numerous fingerprint peaks and a change in the shape of CH-stretch peak are distinct relative to the cytoplasmic region of the cell (Fig. 5, A and B). The fingerprint spectrum from Fig. 4 F (*green box*) is blown up as Fig. 5 A, and peaks at  $785\text{ cm}^{-1}$ ,  $1095\text{ cm}^{-1}$ , and  $1578\text{ cm}^{-1}$  are present in the nuclear spectrum (*blue trace*), as expected, and are much weaker or nonexistent in the cytoplasm (*red trace*). In the high frequency CH-stretch region (Fig. 5 B), a frequency shift is seen at  $2850\text{ cm}^{-1}$  between the cytoplasmic and nuclear spectra. In addition, a change in the shape of the CH-stretch spectrum indicates that lipid content in the nucleus and

cytoplasm is different, which is consistent with previous reports (1,2,6). Finally, taking the difference in the average spectra from nuclei and cytoplasm (Fig. 5 C), we show that B-CARS imaging can resolve differences in vibrational resonances that are spatially segregated between these cellular compartments. The ability to identify nuclei using vibrational spectroscopy is, in and of itself, not surprising and does not exhaustively show the chemical resolving power of the B-CARS spectra shown here. We perform this organelle localization here only as a demonstration that the spectra we obtain are of sufficient quality to do so.

## DISCUSSION

The B-CARS method described herein, which uses a simple, unamplified laser system, is capable of providing full-bandwidth chemical characterization of vibrationally active

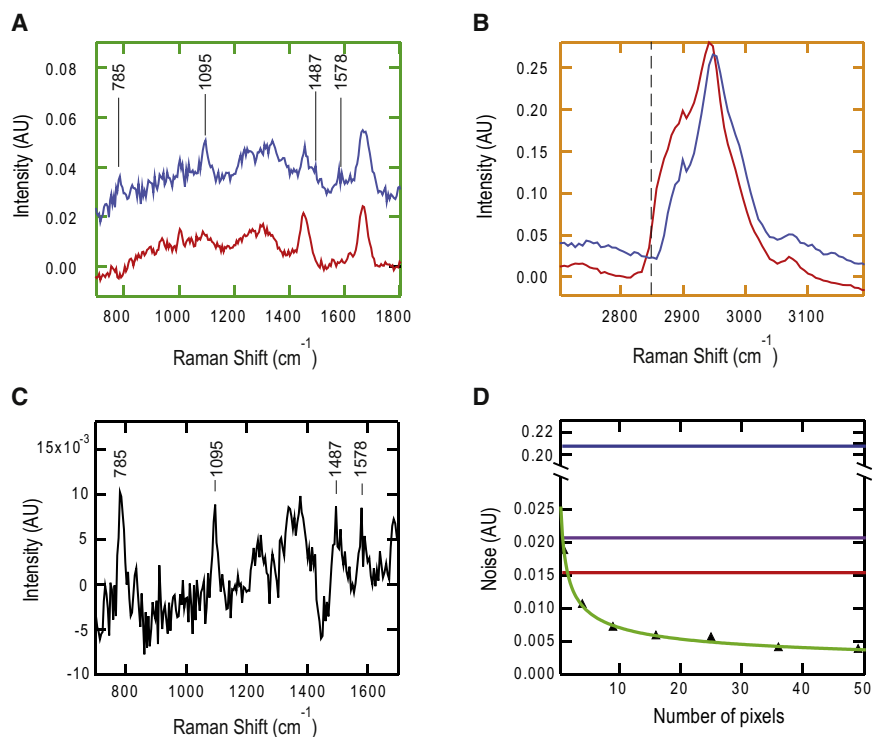


**FIGURE 5** B-CARS microscopy reveals chemical differences between the nuclear and cytoplasmic regions of cells. (A) Spectrum from green box in Fig. 4 F shows fingerprint spectra of nucleus (blue) and cytoplasm (red). Peaks associated with nucleotide bases ( $785\text{ cm}^{-1}$ ,  $1487\text{ cm}^{-1}$ , and  $1587\text{ cm}^{-1}$ ) are labeled in the figure, and are only seen in the blue trace. (B) Spectrum from orange box in Fig. 4 F shows clear differences in the CH-stretch region as well (trace colors are same as for panel A). Nuclear and cytoplasmic spectra are vertically offset for clarity. (C) Difference spectrum between nuclear and cytoplasmic spectra further emphasizes that B-CARS imaging can resolve vibrational differences between these intracellular compartments. (D) Graph showing spectral noise for different Raman resonances in the fingerprint region (red, blue, and purple lines) and showing noise decreases with spatial averaging (black triangles; green line is a fit to guide the eye). The red, purple, and blue lines show the intensity values at which the  $785\text{ cm}^{-1}$ ,  $1660\text{ cm}^{-1}$ , and  $2950\text{ cm}^{-1}$  peaks, respectively, have a  $S/N \approx 1$ . Intersection of these lines with the green curve shows the required spatial (pixel) averaging to achieve  $S/N \approx 1$  for peak detection.

modes in single cells without wavelength tuning or temporal scanning. We have demonstrated chemical imaging from the fingerprint and CH-stretch regions of the Raman spectrum using B-CARS microscopy and shown at least a fivefold improvement in acquisition speed (50 ms/pixel) over spontaneous confocal Raman microspectroscopy. The results shown here are representative of typical data quality, and >50 cells have been imaged under similar conditions. Combined with our resonant signal retrieval method, this microscopy technique is a significant step forward in making label-free chemical characterization of biological samples more widely accessible. In the arena of high-resolution chemical imaging of biological samples, the standard technique has been spontaneous confocal Raman microspectroscopy. B-CARS microscopy, as presented here, fits into this genre and is a significant upgrade in terms of reducing acquisition time and no contamination with fluorescence. In this article, we have increased the spectral window by at least twofold over existing M-CARS to a bandwidth similar to spontaneous Raman spectroscopy with comparable S/N, suggesting that resonantly extracted B-CARS data can be used for subsequent chemical discrimination of biological samples.

Quantitative multivariate analyses with spectroscopic image datasets such as principle component, hierarchical cluster, or linear discriminate analysis require consistent experimental conditions during the entire image acquisition. B-CARS imaging is a point-scanning technique, which makes it susceptible to laser and supercontinuum fluctuations over the acquisition period. As mentioned in the

Materials and Methods, we use a (spatially) local, line-averaged NRB signal for each spatial pixel resonant extraction. By averaging the non-cell-containing pixels in each scanned line, we ameliorate the effects of long-term laser and supercontinuum drift during image acquisition (25 min per image versus 10 s per line). If a single, image-averaged NRB is used for all pixels rather than the line-averaged NRB used here, the low Raman shift region of the spectrum is overwhelmed by a smooth baseline that occludes peaks in that region (see the Supporting Material). Using a line-averaged NRB, it is possible to better recapitulate the true Raman spectrum of each pixel, making the retrieved dataset more appropriate for quantitative analysis.

Though the line-averaged NRB yields improved signal extraction compared to a single NRB spectrum for the entire image, it is not perfectly accurate for every spatial pixel and is not a pure NRB—it is a combination of B-CARS from the glass coverslip and PBS. The result of this imperfect NRB, a residual slowly varying envelope underneath the extracted spectrum, has been previously observed by Rinia et al. (26) in their use of the max-entropy retrieval method of M-CARS spectra of lipid droplets. Beyond thermal drift of the supercontinuum, our B-CARS imaging and signal retrieval system produces repeatable results when imaging the same sample numerous times in the absence of sample damage.

As discussed above, CARS spectra from individual pixels have reduced S/N as compared to spectra averaged over the entire cell (Fig. 2). Because the utility of B-CARS microscopy is full-bandwidth chemical imaging, it is important

to comment on the level of spatial averaging necessary to achieve a detectable signal ( $S/N \geq 1$ ) for specific chemical resonances. In Fig. 5 D (black triangles and green line), we show that the average spectral noise decreases as the number of averaged pixels increases (for the nuclear region in Fig. 4), as expected. As representative Raman modes, noise levels are shown for resonances at  $785\text{ cm}^{-1}$ ,  $1660\text{ cm}^{-1}$ , and  $2950\text{ cm}^{-1}$  where the  $S/N \approx 1$  (Fig. 5 D, red, purple, and blue lines). The places where these lines intersect the green curve in Fig. 5 D show the number of pixels required to generate  $S/N \approx 1$  for these respective spectral features. As expected, the (strong) CH peak requires no averaging, whereas the (weaker)  $1660\text{ cm}^{-1}$  amide I peak and  $785\text{ cm}^{-1}$  DNA peak will require between 2 and 4 pixels, respectively, averaged together to obtain  $S/N \approx 1$ .

We note that this analysis is specific to this dataset and should not be taken as absolute noise and spatial resolution specifications. However, it provides general guidelines about the amount of averaging required to detect characteristic peaks in B-CARS fingerprint spectra. Therefore, one can expect to observe discernible CH-stretch features from single pixels and discernible fingerprint features from  $>5$  pixels averaged together, which corresponds to  $1\text{ }\mu\text{m}^2$  and is roughly the size of mitochondria at the present acquisition settings. Alternatively, reducing the acquisition speed by the same factor will similarly increase the  $S/N$ , allowing for detection of fingerprint features from individual pixels. The ability to observe subtle chemical changes, such as presence or conformation of proteins in a membrane over small spatial regions, is limited by the  $S/N$  of the measurements. If a large number of pixels can be averaged, each containing the same chemical information, then increasingly subtle effects can be detected.

The results presented here may seem surprising in light of recent analysis in the literature comparing to spontaneous confocal Raman. Several studies have quantitatively considered the efficiency of CARS relative to spontaneous Raman scattering (17,45). All of these studies arrive at the same conclusion—CARS gives higher signal only when the product of laser power and analyte concentration is above some threshold. Cui et al. (46) have recently discussed this issue specifically for cellular imaging, showing that, for laser powers conducive to biological imaging at  $800\text{ nm}$ , CARS gives signal equivalent to or greater than spontaneous Raman only for analytes of relatively high local concentration (such as lipids). In the B-CARS works shown here, using  $42\text{ mW}$  total excitation, which is below the physical damage threshold, we are able to obtain full spectra significantly faster than can be done with spontaneous Raman under comparable excitation powers (2,5), as evidenced by the spectra of Figs. 2, 4, and 5.

While this result is not predicted by the quantitative analysis in Cui et al. (48), our findings are reconciled with their work by considering an important difference between our B-CARS approach and their analysis: they consider only

vibrationally resonant CARS (the third term in Eq. 1), while we take advantage of signal from both the resonant and heterodyne mechanisms. The heterodyne mixing contribution (second term in Eq. 1) can substantially increase the CARS signal of interest. This term scales linearly with analyte concentration, thereby increasing detection sensitivity for low concentration analytes beyond that predicted with the resonant contribution alone. The combination of the heterodyne and resonant terms facilitates full spectral acquisition at faster rates and allows B-CARS to acquire images more quickly than spontaneous confocal Raman microspectroscopy at similar excitation powers.

Recent improvements in spontaneous Raman image collection have resulted in considerably reduced vibrational image acquisition rates from biological samples and could be used to improve B-CARS imaging speed as well. These modifications include a fiber bundle multiplex Raman probe (47) and a slit-scanning geometry (48). Both systems use multiplex detection to reduce the effective spectral acquisition time to  $\approx 10\text{ ms}$  by acquiring spectra from  $\approx 100$  confocal pixels simultaneously. Other innovations, such as electron-multiplying charge-coupled devices (EMCCDs), are now being deployed in commercial spontaneous Raman systems, and can obtain spectra in  $<1\text{ ms}$  from materials where there is low background and high tolerance for laser excitation. EMCCDs serve to reduce the impact of CCD read noise and improve signal/noise with relatively fewer photons when read noise is an important contributor to the overall noise. They are less beneficial when a significant background accompanies the signal of interest, such as with CARS or spontaneous Raman imaging of biological samples. In such situations, CCD read noise can be small compared to shot noise from the background, and EMCCDs have a diminished benefit. Finally, potential methods to realize acquisition speed improvements could involve local field enhancement techniques (e.g., surface-enhanced Raman spectroscopy) (49). Surface-enhanced CARS has been demonstrated previously with single molecule detection sensitivity (50) but has not been applied for cellular imaging.

We have shown that B-CARS can be used to obtain full vibrational spectra of similar quality to that obtained with spontaneous Raman but at faster rates. We believe that this will enable wider exploitation of information-rich vibrational spectroscopic imaging for better understanding of biological systems. While the  $50\text{-ms/pixel}$  demonstrated here is certainly a step in the right direction, faster imaging would propel B-CARS further into the mainstream. Living biological systems have been shown to tolerate as much as 10 times more excitation intensity at  $1200\text{ nm}$  than  $800\text{ nm}$  (51) before damage occurs. By shifting the pump-probe light further to the red, one could take advantage of higher permissible power levels and expect potential acquisition rates of 50 times faster than demonstrated here, based on the nonlinear power dependence in the CARS signal.

## CONCLUSIONS

We have demonstrated a B-CARS microscopy system to acquire vibrational spectral maps from single cells. Until now, only spontaneous confocal Raman microspectroscopy has been able to provide complete spatiochemical maps of single cells. The microscopy technique presented here improves the vibrational spectrum acquisition rates and addresses previous challenges to successful implementation of B-CARS microscopy such as the strong NRB and reduced spectral range. At laser powers set just below the physical damage threshold for the cells (0.5 nJ total pulse energy), we can obtain high quality spectra with minimal spatial averaging to generate chemical maps of individual cells. The ability to discriminate between nuclear and cytoplasmic regions of cells is shown and future experiments are aimed at identifying additional organelles and investigating subcellular changes during physiological processes such as differentiation and activation using multivariate analyses.

We believe that B-CARS microscopy, as presented here with at least a fivefold speed improvement, will allow for wider application of Raman spectroscopic imaging to glean information from chemically complex biological systems. With subsequent improvements in laser technology, B-CARS microscopy will enable spatiochemical vibrational imaging at rates comparable with dynamic processes in living cells.

## SUPPORTING MATERIAL

Additional information is available at [http://www.biophysj.org/biophysj/supplemental/S0006-3495\(10\)00977-X](http://www.biophysj.org/biophysj/supplemental/S0006-3495(10)00977-X).

We thank Michael Weiger (National Institute of Standards and Technology (NIST)), Stephan Stranick (NIST), and Hari Shroff (National Institutes of Health) for critical reading of the manuscript and the Biomaterials Group at NIST for helpful discussions.

S.H.P. is supported by a National Research Council NIST Postdoctoral Fellowship, and K.A.A. is supported by award No. P41EB001046 from the National Institutes of Health/National Institute of Biomedical Imaging and Bioengineering.

National Institute of Standards and Technology (NIST): Certain equipment is identified in this article to specify adequately the experimental details. Such identification does not imply recommendation by the National Institute of Standards and Technology, nor does it imply that the equipment is necessarily the best available for this purpose. Official contributions of the National Institute of Standards and Technology—not subject to copyright in the United States.

## REFERENCES

- Matthäus, C., T. Chernenko, ..., M. Diem. 2007. Label-free detection of mitochondrial distribution in cells by nonresonant Raman microspectroscopy. *Biophys. J.* 93:668–673.
- Uzunbajakava, N., A. Lenferink, ..., C. Otto. 2003. Nonresonant confocal Raman imaging of DNA and protein distribution in apoptotic cells. *Biophys. J.* 84:3968–3981.
- Chan, J., S. Fore, ..., T. Huser. 2008. Raman spectroscopy and microscopy of individual cells and cellular components. *Laser Photon. Rev.* 2:325–349.
- Nottingham, I., I. Bisson, ..., L. L. Hench. 2004. In situ spectral monitoring of mRNA translation in embryonic stem cells during differentiation in vitro. *Anal. Chem.* 76:3185–3193.
- Chan, J. W., D. K. Lieu, ..., R. A. Li. 2009. Label-free separation of human embryonic stem cells and their cardiac derivatives using Raman spectroscopy. *Anal. Chem.* 81:1324–1331.
- Chan, J. W., D. S. Taylor, ..., T. Huser. 2006. Micro-Raman spectroscopy detects individual neoplastic and normal hematopoietic cells. *Biophys. J.* 90:648–656.
- Nottingham, I., G. Jell, ..., L. L. Hench. 2004. In situ non-invasive spectral discrimination between bone cell phenotypes used in tissue engineering. *J. Cell. Biochem.* 92:1180–1192.
- Schut, T. C. B., R. Wolthuis, ..., G. J. Puppels. 2002. Real-time tissue characterization on the basis of in vivo Raman spectra. *J. Raman Spectrosc.* 33:580–585.
- Gniadecka, M., P. A. Philipsen, ..., H. C. Wulf. 2004. Melanoma diagnosis by Raman spectroscopy and neural networks: structure alterations in proteins and lipids in intact cancer tissue. *J. Invest. Dermatol.* 122:443–449.
- Kast, R. E., G. K. Serhatkulu, ..., R. Rabah. 2008. Raman spectroscopy can differentiate malignant tumors from normal breast tissue and detect early neoplastic changes in a mouse model. *Biopolymers.* 89:235–241.
- Chan, J. W., and D. K. Lieu. 2009. Label-free biochemical characterization of stem cells using vibrational spectroscopy. *J. Biophoton.* 2:656–668.
- Uzunbajakava, N., A. Lenferink, ..., C. Otto. 2003. Nonresonant Raman imaging of protein distribution in single human cells. *Biopolymers.* 72:1–9.
- van Manen, H. J., Y. M. Kraan, ..., C. Otto. 2005. Single-cell Raman and fluorescence microscopy reveal the association of lipid bodies with phagosomes in leukocytes. *Proc. Natl. Acad. Sci. USA.* 102:10159–10164.
- Chernenko, T., C. Matthäus, ..., M. Diem. 2009. Label-free Raman spectral imaging of intracellular delivery and degradation of polymeric nanoparticle systems. *ACS Nano.* 3:3552–3559.
- Cheng, J. X., Y. K. Jia, ..., X. S. Xie. 2002. Laser-scanning coherent anti-Stokes Raman scattering microscopy and applications to cell biology. *Biophys. J.* 83:502–509.
- Cheng, J. X., and X. S. Xie. 2004. Coherent anti-Stokes Raman scattering microscopy: Instrumentation, theory, and applications. *J. Phys. Chem. B.* 108:827–840.
- Tolles, W. M., J. W. Nibler, ..., A. B. Harvey. 1977. Review of theory and application of coherent anti-Stokes Raman spectroscopy (CARS). *Appl. Spectrosc.* 31:253–271.
- Duncan, M. D., J. Reintjes, and T. J. Manuccia. 1982. Scanning coherent anti-Stokes Raman microscope. *Opt. Lett.* 7:350–352.
- Zumbusch, A., G. R. Holtom, and X. S. Xie. 1999. Three-dimensional vibrational imaging by coherent anti-Stokes Raman scattering. *Phys. Rev. Lett.* 82:4142–4145.
- Evans, C. L., E. O. Postma, ..., X. S. Xie. 2005. Chemical imaging of tissue in vivo with video-rate coherent anti-Stokes Raman scattering microscopy. *Proc. Natl. Acad. Sci. USA.* 102:16807–16812.
- Kee, T. W., and M. T. Cicerone. 2004. Simple approach to one-laser, broadband coherent anti-Stokes Raman scattering microscopy. *Opt. Lett.* 29:2701–2703.
- Yakovlev, V., and G. I. Petrov. 2005. Enhancing red-shifted white-light continuum generation in optical fibers for applications in nonlinear Raman microscopy. *Opt. Express.* 13:1299–1306.
- Cheng, J.-X., A. Volkmer, ..., X. S. Xie. 2002. Multiplex coherent anti-Stokes Raman scattering microspectroscopy and study of lipid vesicles. *J. Phys. Chem. B.* 106:8493–8498.
- Kano, H., and H. O. Hamaguchi. 2005. Vibrationally resonant imaging of a single living cell by supercontinuum-based multiplex coherent

- anti-Stokes Raman scattering microspectroscopy. *Opt. Express*. 13:1322–1327.
25. Kano, H., and H. O. Hamaguchi. 2006. In-vivo multi-nonlinear optical imaging of a living cell using a supercontinuum light source generated from a photonic crystal fiber. *Opt. Express*. 14:2798–2804.
  26. Rinia, H. A., K. N. J. Burger, ..., M. Müller. 2008. Quantitative label-free imaging of lipid composition and packing of individual cellular lipid droplets using multiplex CARS microscopy. *Biophys. J.* 95:4908–4914.
  27. Bonn, M., M. Müller, ..., K. N. J. Burger. 2009. Imaging of chemical and physical state of individual cellular lipid droplets using multiplex CARS microscopy. *J. Raman Spectrosc.* 40:763–769.
  28. Petrov, G. I., R. Arora, ..., M. O. Scully. 2007. Comparison of coherent and spontaneous Raman microspectroscopies for noninvasive detection of single bacterial endospores. *Proc. Natl. Acad. Sci. USA*. 104:7776–7779.
  29. Pestov, D., X. Wang, ..., M. O. Scully. 2008. Single-shot detection of bacterial endospores via coherent Raman spectroscopy. *Proc. Natl. Acad. Sci. USA*. 105:422–427.
  30. Lee, Y. J., S. H. Parekh, ..., M. T. Cicerone. 2010. Optimized continuum from a photonic crystal fiber for broadband time-resolved coherent anti-Stokes Raman scattering. *Opt. Express*. 18:4371–4379.
  31. Oron, D., N. Dudovich, and Y. Silberberg. 2003. Femtosecond phase-and-polarization control for background-free coherent anti-Stokes Raman spectroscopy. *Phys. Rev. Lett.* 90:213902.
  32. Lee, Y. J., and M. T. Cicerone. 2009. Single-shot interferometric approach to background free broadband coherent anti-Stokes Raman scattering spectroscopy. *Opt. Express*. 17:123–135.
  33. Vartiainen, E. M. 1992. Phase retrieval approach for coherent anti-Stokes-Raman scattering spectrum analysis. *J. Opt. Soc. Am. B*. 9:1209–1214.
  34. Liu, Y. X., Y. J. Lee, and M. T. Cicerone. 2009. Broadband CARS spectral phase retrieval using a time-domain Kramers-Kronig transform. *Opt. Lett.* 34:1363–1365.
  35. Lieber, C. A., and A. Mahadevan-Jansen. 2003. Automated method for subtraction of fluorescence from biological Raman spectra. *Appl. Spectrosc.* 57:1363–1367.
  36. Arora, R., G. I. Petrov, and V. V. Yakovlev. 2008. Analytical capabilities of coherent anti-Stokes Raman scattering microspectroscopy. *J. Mod. Opt.* 55:3237–3254.
  37. Rinia, H. A., M. Bonn, ..., E. M. Vartiainen. 2007. Quantitative CARS spectroscopy using the maximum entropy method: the main lipid phase transition. *ChemPhysChem*. 8:279–287.
  38. Liu, Y. X., Y. J. Lee, and M. T. Cicerone. 2009. Fast extraction of resonant vibrational response from CARS spectra with arbitrary nonresonant background. *J. Raman Spectrosc.* 40:726–731.
  39. Vartiainen, E. M., H. A. Rinia, ..., M. Bonn. 2006. Direct extraction of Raman line-shapes from congested CARS spectra. *Opt. Express*. 14:3622–3630.
  40. Hellwarth, R. W. 1977. Third-order optical susceptibilities of liquids and solids. *Prog. Quantum Electron.* 5:1–68.
  41. Xie, C., M. A. Dinno, and Y. Q. Li. 2002. Near-infrared Raman spectroscopy of single optically trapped biological cells. *Opt. Lett.* 27:249–251.
  42. Liang-da, C., A. Masahiro, and H. O. Hamaguchi. 2009. Study of the Raman spectroscopic signature of life in mitochondria isolated from budding yeast. *J. Raman Spectrosc.* 41:2–3.
  43. Jeney, F., E. Bazsó-Dombi, ..., I. Z. Nagy. 2000. Cytochemical studies on the fibroblast-preadipocyte relationships in cultured fibroblast cell lines. *Acta Histochem.* 102:381–389.
  44. Nan, X. L., J. X. Cheng, and X. S. Xie. 2003. Vibrational imaging of lipid droplets in live fibroblast cells with coherent anti-Stokes Raman scattering microscopy. *J. Lipid Res.* 44:2202–2208.
  45. Begley, R. F., A. B. Harvey, and R. L. Byer. 1974. Coherent anti-Stokes Raman spectroscopy. *Appl. Phys. Lett.* 25:387–390.
  46. Cui, M., B. R. Bachler, and J. P. Ogilvie. 2009. Comparing coherent and spontaneous Raman scattering under biological imaging conditions. *Opt. Lett.* 34:773–775.
  47. Gift, A. D., J. Y. Ma, ..., D. Ben-Amotz. 1999. Near-infrared Raman imaging microscope based on fiber-bundle image compression. *J. Raman Spectrosc.* 30:757–765.
  48. Hamada, K., K. Fujita, ..., S. Kawata. 2008. Raman microscopy for dynamic molecular imaging of living cells. *J. Biomed. Opt.* 13:044027.
  49. De Angelis, F., G. Das, ..., E. Di Fabrizio. 2010. Nanoscale chemical mapping using three-dimensional adiabatic compression of surface plasmon polaritons. *Nat. Nanotechnol.* 5:67–72.
  50. Koo, T. W., S. Chan, and A. A. Berlin. 2005. Single-molecule detection of biomolecules by surface-enhanced coherent anti-Stokes Raman scattering. *Opt. Lett.* 30:1024–1026.
  51. Yakovlev, V. V. 2003. Advanced instrumentation for non-linear Raman microscopy. *J. Raman Spectrosc.* 34:957–964.